

Multi-wavelength observations of the massive YSO RAFGL7009S*

E. Dartois¹, M. Gerin², and L. d’Hendecourt³

¹ Institut de RadioAstronomie Millimétrique (UPS2074), 300 Rue de la piscine, 38406 Saint Martin d’Hères, France

² Ecole Normale Supérieure (UMR8540), 24 Rue Lhomond, 75231 Paris, France

³ Université Paris XI, Institut d’Astrophysique Spatiale – CNRS (UMR8617), Bâtiment 121, 91405 Orsay Cedex, France

Received 29 March 2000 / Accepted 6 July 2000

Abstract. We present multi-wavelength observations of the young stellar object RAFGL7009S. The analysis combines single dish (IRAM 30m), interferometric (Plateau de Bure Interferometer), as well as infrared (UKIRT and ISO) observations. We use those data to globally describe the source (Spectral Energy Distribution, density) and its environment. We also derive the position of the central object (associated with the HII region) to 1'' precision using the interferometer observations. We have observed HDO and CH₃OD in single dish measurements and derive the D/H ratio for water and methanol in the gas phase. Laboratory experiments allow us to derive upper limits to the enrichment of the same species in the solid phase. It is argued that CH₃OH seems to be a good tracer for grain deuterium enrichment in the environment of RAFGL7009S. Observations of HCN and HNC isomers indicate that along the line of sight, two velocity independent temperature regions coexist.

Key words: ISM: dust, extinction – ISM: individual objects: RAFGL70009S – infrared: ISM: continuum – infrared: ISM: lines and bands

1. Introduction

The determination of the chemical composition of the dust in dense clouds is of prime importance for the evaluation of its role in the thermal and chemical evolution of the condensations, leading eventually to collapse. Indeed, whereas in previous stages of the cloud contraction the chemistry is driven by gas phase neutral-neutral or ion-molecule chemical reactions (e.g. Turner et al. 1999; Herbst & Leung 1990; Langer &

Graedel 1989), at later times, the grains in dense cores ($n_{H_2} > 10^5 \text{ cm}^{-3}$) will strongly interact with the gas, promoting a gas-grain chemistry (Willacy & Millar 1998; Bergin et al. 1995; Hasegawa & Herbst 1993). In this phase the refractory grains provide a surface on which gas phase molecules can stick and react, through grain surface chemistry as well as cosmic ray or UV photons induced photo-chemistry (Shalabeia et al. 1998; Charnley et al. 1992; d’Hendecourt et al. 1985; Lacy et al. 1984; Tielens & Hagen 1982). The way to derive the dust chemical composition in dense clouds is to observe strong infrared emitters which provide a background, or embedded sources, that allow us to observe the dust in absorption against the continuum (Willner et al. 1982). The best candidates for such studies are generally embedded young stellar objects which have just started to ignite in the cloud that gave birth to them. The young star then allows us to probe the parent cloud environment which displays strong absorption lines in the mid infrared associated with the vibration of molecules trapped in ice mantles lying on top of the refractory grains (d’Hendecourt 1984; Hagen et al. 1980; Allamandola et al. 1980).

These absorption features are in some cases so deep that they clearly show that the solid phase represents a major part of the clouds refractory molecular mass. Unfortunately, the continuum generated by the embedded object is not spatially extended and we can only probe along the narrow beam in front of the object as the dust features are observed in absorption in such objects.

In order to investigate the geometry of the objects as well as some gas phase molecules released in the process of solid volatiles evaporation, one can use the millimetre and sub-millimetre wavelength range. In this range, we deal with emission and absorption spectroscopy as the molecular excitation temperature is lower than, or equal to, the gas kinetic temperature. The dust thermal radiation provides some continuum emission, generally in the Rayleigh-Jeans domain, and is usually optically thin, and much weaker than the line emission. We can then map the emission from transitions to investigate the source geometry.

Among the most massive infrared objects studied for their solid phase features is the class I, late O or early B star, named RAFGL7009S. This object is, together with W33A, one of the most extinguished source in terms of ice mantle absorptions. It has been observed with the Infrared Space Observatory

Send offprint requests to: E. Dartois (dartois@ias.fr)

* Based on observations carried out with the IRAM 30m telescope, Plateau de Bure interferometer, Infrared space Observatory (ISO) and United Kingdom Infrared Telescope (UKIRT). IRAM is supported by INSU/CNRS (France), MPG (Germany) and IGN (Spain). ISO is an ESA project with instruments funded by ESA Member States (especially the PI countries: France, Germany, the Netherlands and the United Kingdom) and with the participation of ISAS and NASA. The United Kingdom Infrared Telescope is operated by the Joint Astronomy Centre on behalf of the U.K. Particle Physics and Astronomy Research Council.

Short and Long Wavelengths Spectrometers (hereafter SWS and LWS) and numerous studies have been reported in the infrared (d'Hendecourt et al. 1996; Dartois et al. 1998; Dartois et al. 1999).

In this paper we present multi-wavelength (infrared and millimetre) observations of the source RAFGL7009S. These observations include single dish and interferometer observations. We begin by briefly describing the observations. We discuss in Sect. 3 the global properties of RAFGL7009S, which include its spectral energy distribution, the source continuum emission and the mean H₂ density in the object as seen by single dish observations. We then present (Sect. 4) the symmetric top molecules (plus methanol) observations, recorded with the IRAM 30m telescope and, for the methyl cyanide molecule, with the Plateau de Bure Interferometer (hereafter PdBI).

In the next section (Sect. 5) we focus on deuterated species observations. We compare the gas phase observations of hydrides and their deuteride parent to solid phase observations and laboratory experiments. We discuss the implications. The case of HCN and HNC isomers is discussed in the next section (Sect. 6).

2. Observations

The observations presented in this paper were obtained with several instruments and several runs. The millimetre wavelength observations were carried with the 30m telescope during three periods (8-12 August 1997 and 26 July- 3 August 1998; 16-19 May 1999). The spectra were obtained in the Position Switching mode, with a reference position located 300'' south of the central source. This reference position was observed in Frequency Switching mode, and showed no ¹³CO(2→1) emission down to a rms noise level of 0.38 K. A comparison between ¹³CO(2→1) spectra obtained at the central position of the source in both position switching and frequency switching mode showed they were similar, at a similar noise level.

With the Plateau de Bure Interferometer, located in the French Alps, we mapped the ¹³CO 2→1 and 1→0 transitions as well as CH₃CN 12→11 and 6→5 transitions.

Infrared observations presented in this paper were recorded with the United Kingdom Infrared Telescope (UKIRT) equipped with the CGS4 detector, and Short Wavelength Spectrometer observations on board of the Infrared Space Observatory (ISO, Kessler et al. 1996).

3. Global properties of RAFGL7009S

3.1. Mass distribution

RAFGL7009S is classified as an ultra compact HII region, which implies small extensions and high densities. The observations gathered by McCutcheon et al. (1991) on this source indicate the presence of a molecular outflow associated with the source. The H₂ column density is extremely high ($\sim 5.3 \times 10^{22} \text{ cm}^{-2}$).

We propose, in this section, to obtain a global overview of the mass distribution at a given temperature in this object

using the combination of IRAS data (at 12, 25, 60 and 100 μm) and the one obtained by McCutcheon et al. (1995) at larger wavelengths (450, 800 and 1100 μm). The flux emitted by the grains is related by an integral equation to the mass distribution. Under some assumptions, this equation can be inverted.

According to Kirchoff's law, the monochromatic emission j_ν of dust grains is related to their mean absorption coefficient per unit mass ($\text{g}^{-1} \text{ cm}^2$) κ_ν (Xie et al. 1993):

$$j_\nu = \rho_d \kappa_\nu B_\nu(T) \quad (\text{erg.s}^{-1} \text{ Hz}^{-1} \text{ sr}^{-1} \text{ cm}^{-3})$$

where ρ_d (g cm^{-3}) is the grain mass density and $B_\nu(T)$ is the blackbody Planck function. We can define $M(\mathbf{r}, T)$ ($\text{g cm}^{-3} \text{ K}^{-1}$) the dust mass per unit volume and at temperature T located at \mathbf{r} in the cloud under consideration. The emerging flux is then given by:

$$F(\nu) = \int_0^\Omega B_\nu(2.7\text{K}) e^{-\tau_\nu} d\Omega + \kappa_\nu \int_0^\infty \int_0^\Omega \int_0^L M(\mathbf{r}, T) B_\nu(T) e^{-\tau_\nu} dl d\Omega dT$$

with

$$\tau_\nu = - \int_0^l \rho(\mathbf{r}) \kappa_\nu dl'$$

where L is the spatial extent of the cloud along the line of sight, Ω is the solid angle subtended by the cloud, $\rho(\mathbf{r})$ is the density at the position \mathbf{r} .

The first part of the above equation represents the cosmological background contribution to the observed flux.

We can define:

$$W(\nu, T) = D^2 \int_0^\Omega \int_0^L M(\mathbf{r}, T) e^{-\tau_\nu} dl d\Omega$$

where $W(\nu, T)$ is the dust mass distribution at a given temperature and D the distance to the source (≈ 3.3 kpc).

In the optically thin limit, $\tau_\nu \ll 1$, hence $e^{-\tau_\nu} \sim 1$ and the thermal radiation escapes freely from the whole cloud. In this limit, the flux equation becomes independent of the cloud geometry and mass spatial distribution. With a position switched observation we can get rid of the background term (this one is however negligible if the source is a strong emitter). We have then:

$$F(\nu) = \frac{\kappa_\nu}{D^2} \int_0^\infty W(T) B_\nu(T) dT.$$

We look for $W(T)$, the mass distribution at the temperature T , in the surrounding envelope. To do this, we ignore the source geometry which no longer enters explicitly in the calculation. We must therefore invert the previous equation. Following Xie et al. (1993), we use Chen's Möbius modified theorem (1990). This theorem expresses the fact that $W(T)$ is given by:

$$W(T) = x \sum_{n=1}^{\infty} \frac{\mu(n)}{n} f\left(\frac{x}{n}\right) \quad ; \quad x = \frac{h}{kT}$$

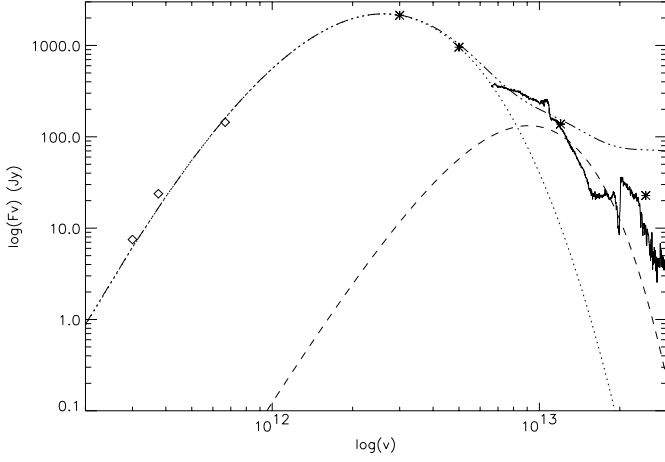


Fig. 1. Spectral energy distribution in the line of sight of RAFGL7009S. The diamonds are measurements by McCutcheon et al., the stars are the IRAS filters measurements (at 12, 25, 60 and 100 μm) and the continuous spectrum was obtained with the Short Wavelength Spectrometer on board ISO. The dotted line corresponds to the functional form $G(\nu)$ fitted to the long wavelength range data, and used in the temperature inversion (see text). The dashed line represent an estimate of the flux at higher frequency not used in the inversion as it is not in the optically thin region, and the dot-dashed line is the sum of the two contributions plus a higher temperature blackbody ($\sim 500\text{K}$) as discussed in the text.

where $\mu(n)$ is the Möbius function that equals 1 if $n=1$, $(-1)^r$ if n possesses r distinct prime factors and otherwise $\mu(n)=0$. We assume that the variation of the emissivity with frequency follows a power law, $\kappa_\nu = \kappa_0 \nu^\alpha$. Writing $x = (h/kT)$, we define the function $f(x)$ as the inverse Laplace transform of the flux:

$$f(x) = L^{-1}(C \nu^{-3} F(\nu)/\kappa_\nu)$$

with

$$C = D^2 c^2 / 2h \quad \kappa_\nu = \kappa_0 \nu^\alpha.$$

To fully cover a range of possible values for the grain emissivity (e.g. Koike et al. 1995), we use two different absorption coefficients for the grains.

The first is given by Xie et al. (1993) and equals $\kappa_\nu (\text{cm}^2 \text{g}^{-1}) = \kappa_0 \nu^{3/2} = 7.9 \times 10^{-18} \nu^{3/2}$. The second is provided by more recent measurements done by Boulanger et al. (1996) leading to $\tau/N_H \sim 10^{-25} \times (\lambda/250 \mu\text{m})^{-2}$. Assuming that the ratio $\rho_{\text{gas}}/\rho_{\text{dust}} \sim 100$, we obtain $\kappa_\nu (\text{cm}^2 \text{g}^{-1}) = \kappa_0 \nu^2 = 4.15 \times 10^{-24} \nu^2$ in the second case.

Observations in the far infrared/millimeter range are fitted using the functional form $G(\nu) = A \nu^{\beta} \exp(-B \nu^{1/2})$ (proposed by Xie et al. 1993) which seems adapted to the observations in this wavelength region and is analytically invertible by the Laplace Transform. The best fit parameters to the data leads to $A = 3.258 \times 10^{-78}$ and $B = 8.673 \times 10^{-6}$, $\beta = 7$ where $F(\nu)$ and ν are given in Jansky and Hertz, respectively (see Fig. 1).

With these parameters we must then use the inverse Laplace Transform of the function $A C \nu^{\beta-3-\alpha} e^{-B \nu^{1/2}}$ (we replaced $F(\nu)$ by the functional form $G(\nu)$ in the previous

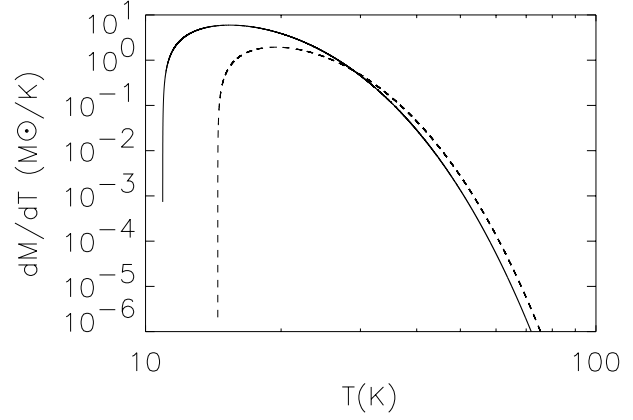


Fig. 2. Mass distribution at a given temperature resulting from the inversion on the long wavelength range data: solid line $\alpha=2$, dashed line $\alpha=3/2$.

equation). Using the Laplace transform properties¹, the special functions $L(x^{-3/2} e^{-\gamma/4x}) = 2\sqrt{\frac{\pi}{\gamma}} e^{-(\gamma s)^{1/2}}$ and $L(x^{-1/2} e^{-\gamma/4x}) = 2\sqrt{\pi} s^{-1/2} e^{-(\gamma s)^{1/2}}$, the inverse transforms we need to build $W(T)$ with $\alpha=3/2$ and 2 are respectively:

$$f(x) = \frac{D^2 c^2 A}{2h \kappa_0} \frac{1}{8} e^{-\frac{B^2}{4x}} (-15x^{-7/2} + \frac{45}{2} B^2 x^{-9/2} - \frac{15}{4} B^4 x^{-11/2} + \frac{1}{8} B^6 x^{-13/2})$$

$$\frac{D^2 c^2 A}{2h \kappa_0} = 2042.4$$

$$f(x) = \frac{D^2 c^2 A}{2h \kappa_0} \frac{1}{4} e^{-\frac{B^2}{4x}} (15x^{-7/2} - 5B^2 x^{-9/2} + \frac{1}{4} B^4 x^{-11/2})$$

$$\frac{D^2 c^2 A}{2h \kappa_0} = 33712.2.$$

The results of this inversion are shown in Fig. 2 for the two different values used for α .

Integrating $W(T)$ over the temperature, the derived dust mass in the envelope is equal to 21.8 M_\odot ($\alpha=3/2$) and 43.4 M_\odot ($\alpha=2$). For both grain models, the bulk of the dust ($> 95\%$) is very cold (< 33 and 29 K) for $\kappa_\nu \propto \nu^{3/2}$ and $\propto \nu^2$ respectively.

The law of variation of the emissivity with frequency drives the efficiency by which a grain absorbs and emits radiation. The higher the emissivity index is at long wavelength, the lower is the equilibrium temperature of the dust grains. We must therefore invoke more mass of matter to account for the same flux with a steeper emissivity law if we only fit the optically thin part of the emission. The observed flux is related to the emissivity by an integral equation containing a given fixed point (κ_0) and a slope. Although the fixed point has to be determined carefully, α , is a fundamental parameter to constrain if we want to derive a reliable mass estimate.

¹ $L\left(\frac{d^n}{dx^n} f(x)\right) = s^n F(s)$

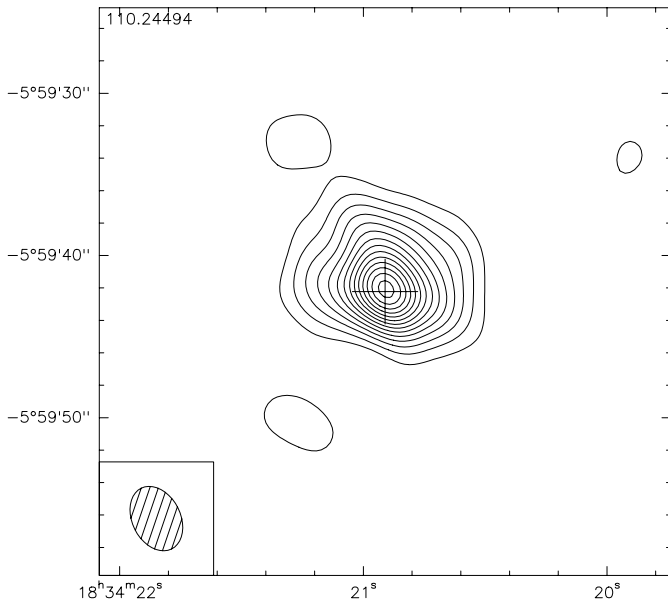


Fig. 3. Continuum map of RAFGL7009S at 110.2 GHz, as derived by interferometer observations. The contours levels are 3mJy/Beam, representing the 3σ level. The lower left corner represents the half power beam size of the clean beam

The continuous spectrum presented in Fig. 1 in the high frequency domain is the one measured by the Infrared Space Observatory (ISO). It shows an infrared excess. The IRAS $12\mu\text{m}$ measurement is considerably lower than the continuum. This is due to the presence of the strong silicate absorption as well as the water ice librational mode (hindered rotation in the solid phase). The presence of other molecules in the solid phase does not allow the spectrum to be fitted with a simple curve. However, the residual emission after subtraction of the fitted profile in the long wavelength part of the spectrum corresponds roughly to a blackbody of 80-120K assuming an emissivity $\propto \nu^{3/2}$ (dashed line in Fig. 1)).

The numerous absorptions, from both gas and solid phases, in the near and mid-infrared are discussed elsewhere (d’Hendecourt et al. 1996; Dartois et al. 1998). They appear on a continuum which can be attributed to a blackbody of 500K-1000K, emitted by dust grains located near the protostar(s).

When we performed the inversion, we did not take into account the short wavelength part of the spectrum (represented by the dashed fit in the Fig. 1) as the optically thin hypothesis is no longer valid. The inversion of the complete spectrum would require solving a more complex integral equation which needs to have source geometry well specified. Solving the equation in its general form will enhance the contribution of higher temperatures in the dust mass distribution presented in Fig. 2, lowering the proportion of very cold dust. However, the major part will still reside in the low temperature regime.

The continuum emission at 110.2 GHz is shown in Fig. 3. The integrated flux is 100 mJy, with an accuracy of 10%, assuming no loss due to the interferometer filtering (Half Power Beamsize $\approx 44''$). The dust envelope appears to indicate a sim-

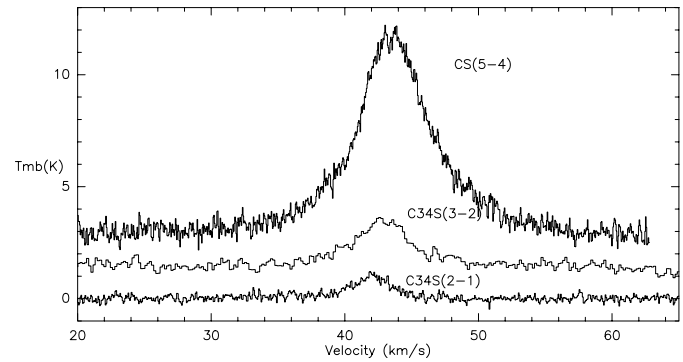


Fig. 4. CS and C^{34}S spectra observed towards RAFGL7009S.

ple power law density distribution. This finding contrasts with the CO gas phase observation of this source.

3.2. Mean H_2 density

Using the 30m telescope, we observed $\text{C}^{34}\text{S}(2\rightarrow 1)$, $\text{C}^{34}\text{S}(3\rightarrow 2)$ and $\text{CS}(5\rightarrow 4)$ towards RAFGL7009s. The intensity ratio is $\text{C}^{34}\text{S}(2\rightarrow 1)/\text{C}^{34}\text{S}(3\rightarrow 2) = 0.6$. Using an LVG model (P. Schilke, private communication), we performed a statistical equilibrium calculation, using a C^{34}S column density of $3.3 \times 10^{13} \text{cm}^{-2}$, and a line width of 5.5 km/s. The observed intensities are consistent with a high density ($n(\text{H}_2) > 10^6 \text{cm}^{-3}$). Assuming a terrestrial isotopic ratio for sulfur, we obtained a constraint on the kinetic temperature by comparing the $\text{CS}(5-4)$ and $\text{C}^{34}\text{S}(3-2)$ data: the gas is quite cold, with $T_K \sim 20 \text{K}$. We also observed two lines of para-formaldehyde, which lead to the same conclusion.

4. CH_3CN , CH_3CCH and CH_3OH

We have measured transitions of several symmetric top molecules as well as methanol lines in the line of sight toward RAFGL7009S. The resulting set of observations has to be separated in two parts. Indeed, during interferometric observations of the $\text{CH}_3\text{CN} 12\rightarrow 11$ transitions, we find evidence for a shift of $\sim 3''$ between the position used in the ISO observations and the first observations done at the IRAM 30m telescope. The true position of the (compact HII) source, which coincide with the continuum emission, is then:

RA(2000) 18h34m20.91s

DEC(2000) -05°59'42.22''

This change has little effect on the discussion of absorption measurements (such as the ones in the solid or gas phase transitions made with ISO) as the flux scales proportionally, and the line to continuum ratio remains constant. However, for millimetre data, it is important to note this difference when comparing lines observed before and after this pointing “correction”. The observations observed before the new pointing position are: for CH_3CN the $6\rightarrow 5$ and $12\rightarrow 11$ transitions; for CH_3CCH the $6\rightarrow 5$ transition; for CH_3OH the $2\rightarrow 1$, $3\rightarrow 2$ and $5\rightarrow 4$ (measured before and after the new position was known) transitions.

4.1. Analysis: The modified rotational diagram

Rather than the classical rotational diagram method (e.g. Cummins et al. 1986), in which one assumes the lines to be optically thin we prefer to use a simple χ^2 minimisation to estimate the basic molecular parameters such as the rotational temperature, column density and source size.

The temperature T_{line} as observed with a telescope with a Gaussian beam and pointing toward a Gaussian shaped emitting source is given by:

$$T_{line} = \frac{\theta_{source}^2}{\theta_{source}^2 + \theta_{beam}^2} T_{rot} (1 - e^{-\tau(\nu)})$$

where $\tau(\nu)$ is given by:

$$\tau(\nu) = \frac{\phi(\nu) A_{ul} c^2}{8\pi\nu^2} \left(\exp\left(\frac{h\nu}{kT_{rot}}\right) - 1 \right) n_u$$

$$N_u = g_u \exp\left(\frac{-E_u}{kT_{rot}}\right) \frac{N}{Q(T_{rot})}$$

where $\phi(\nu)$ is the normalised line shape of the transition (assumed here to be Gaussian), T_{rot} the rotational excitation temperature, A_{ul} the Einstein coefficient of the transition, ν the frequency of the transition, N the total number of molecules, N_u the number in the upper state, g_u its degeneracy and E_u the upper state energy.

In the radio range one often replaces $\exp\left(\frac{h\nu}{kT_{rot}}\right)$ by $1 + \frac{h\nu}{kT_{rot}}$. When $\tau \ll 1$, in the classical rotation diagram there exist a linear relationship between the logarithm of the integrated temperature of the line (generally named W) and E_u/T_{rot} , with an axis intercept defined by $\frac{N}{Q(T_{rot})}$ (see for example Cummins et al. 1986). Fitting a slope to this curve gives access to both T_{rot} and $\frac{N}{Q_{rot}}$. However, this method presents two major disadvantages:

- for molecules whose transitions are blended, the evaluation of W is difficult to perform and can become very tricky. Examples of this effect are given for J+1(0)→J(0) and J+1(1)→J(1) transitions of symmetric top molecules such as CH₃CN and CH₃CCH (e.g. Hatchell et al. 1998), or for molecules like HCOOH, or also the 96GHz 2→1 CH₃OH lines (see Fig. 8).
- some lines can suffer from saturation even when the antenna temperature is low (due to the beam dilution) and the temperature derived in the rotation diagram is then not reliable.

These two reasons lead us to analyse the data by generating models with known parameters and performing a maximum likelihood minimisation to determine the best parameters. In particular, this takes into account any line saturation. It is an intermediate method between the purely optically thin assumption and LVG calculations which also involve some approximations. We thus maximize the function:

$$L(T, N, \theta_{source}) = \prod_{i=1}^N \exp\left(-\frac{1}{2} \frac{(y(i)_{model} - y(i)_{observed})^2}{\sigma^2}\right)$$

where σ is the rms noise, T the rotational temperature and θ_{source} the source extension (full width at half maximum), assuming a Gaussian distribution pattern. The maximum of the function gives the best values for the parameters T , N and θ_{source} and the contours at 1% of the maximum allow to derive the extent of the 3σ confidence range in these parameters. We proceed in two steps to estimate the correct value of σ . We first calculate the likelihood function with the sigma estimated from the noise of the spectrum. Then, we estimate the standard deviation σ from the difference between our best model and the observed spectrum. In this way we also partly take into account the uncertainties due to model imperfections.

If the maximum likelihood function is well-behaved, each probability contour has the shape of a distorted ellipsoid (“boomerang like”) in a three parameter space minimisation. Except for the case for the optically thin lines, this is the case in our calculations. In the optically thin case it is not possible to differentiate between column density effects and beam dilution effects as these two quantities are strongly correlated. The line intensity is a function of the product of the opacity and dilution factor of the source in the beam.

Unless otherwise stated, in this paper, when no source size is explicitly given, we assumed $\frac{\theta_{source}^2}{\theta_{source}^2 + \theta_{beam}^2} = 1.$, performing the minimisation in a two parameter space (T,N). If the source size can be estimated by other means, the column density has to be corrected by this factor.

The observed spectra are displayed in Figs. 6 to 8, together with the corresponding modelled best spectrum, generated using the parameters derived from the maximum likelihood minimisation.

4.2. CH₃CN

The Plateau de Bure interferometer maps of CH₃CN, are shown in Fig. 5a and 5b. In the 12→11 transitions, the source has an extent of about 1 arc-second. In the optically thin limit, the column densities for CH₃CN given in the caption of Fig. 6 have then to be enhanced by a (sometimes very large) factor $\frac{\theta_{source}^2 + (10 \times 240 / \text{frequency(GHz)})^2}{\theta_{source}^2}$, corresponding to the beam dilution.

An extension in the E-W direction is clearly visible in both maps at 3mm (6-5) and 1mm (12-11). This structure is more pronounced in the CH₃CN(6→5). We associate this component with the molecular outflow known to be present in this source at larger scales (Shepherd & Churchwell 1996). The absence of a symmetrical counterpart might imply there exist a difference in the densities in which the jet expands for the other component.

4.3. CH₃CCH

The observed spectra of methyl acetylene and model fit are displayed in Fig. 7. We believe methyl acetylene CH₃CCH to be also found in a compact region of roughly the same extent as for methyl cyanide with therefore the same correction to be

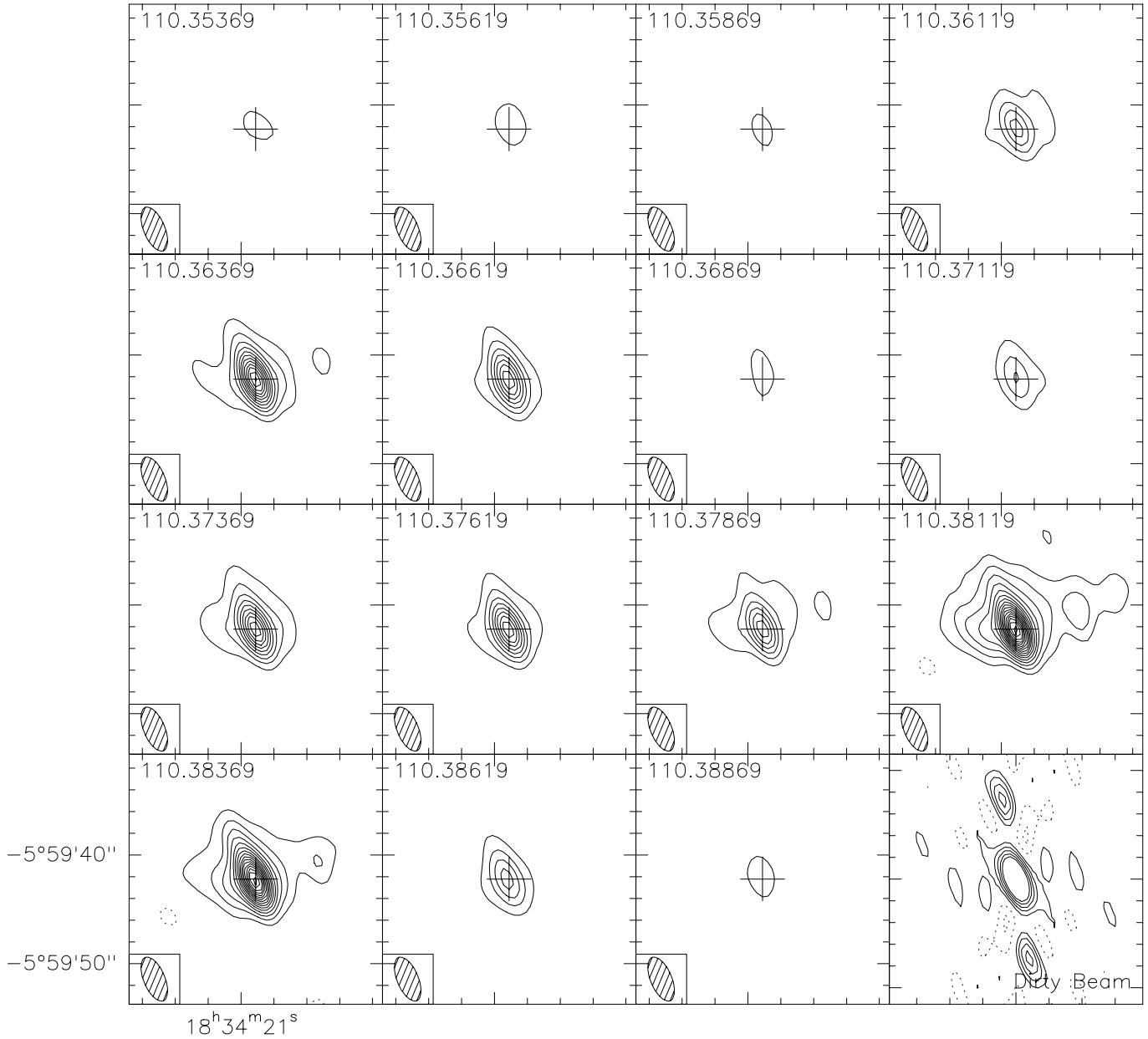


Fig. 5a. Plateau de Bure interferometric map of RAFGL7009S in the CH_3CN 6 \rightarrow 5 transitions. The lowest contour levels and the increment are 20 mJy/beam. Also shown is the dirty beam (bottom right) resulting from the observations and the half power clean beam ($4.31'' \times 1.94''$) in the lower left of each channel. The frequency is indicated in the top left corner of each panel.

applied to the column density estimates, as is generally the case in ultra compact HII regions (Hatchell et al. 1998).

To estimate the physical parameters (T, N) for this molecule, we used the optically thin limit estimate as we do not see clear evidence for saturation in the maximum likelihood minimisation. If the lines are thermalised, due to the lower temperature, the molecule emission must be more extended than for the methyl cyanide case. From the derived column densities presented in Fig. 7, and assuming the kinetic temperature is the same for both transitions, we estimate the source size around 6-10''.

4.4. CH_3OH

In order to derive the best column densities, it is crucial to estimate the source size as accurately as possible. Using the interferometric maps, we showed, in Sect. 4 above, that the millimetre compact emitting region is located 3'' away from the ISO position which was used in the first millimetre observations as the map centre. This means that we have to correct the observed antenna temperature by a factor that takes into account the shape of the 30m telescope beam at a given wavelength and the new accurate position in order to make suitable comparisons between the data.

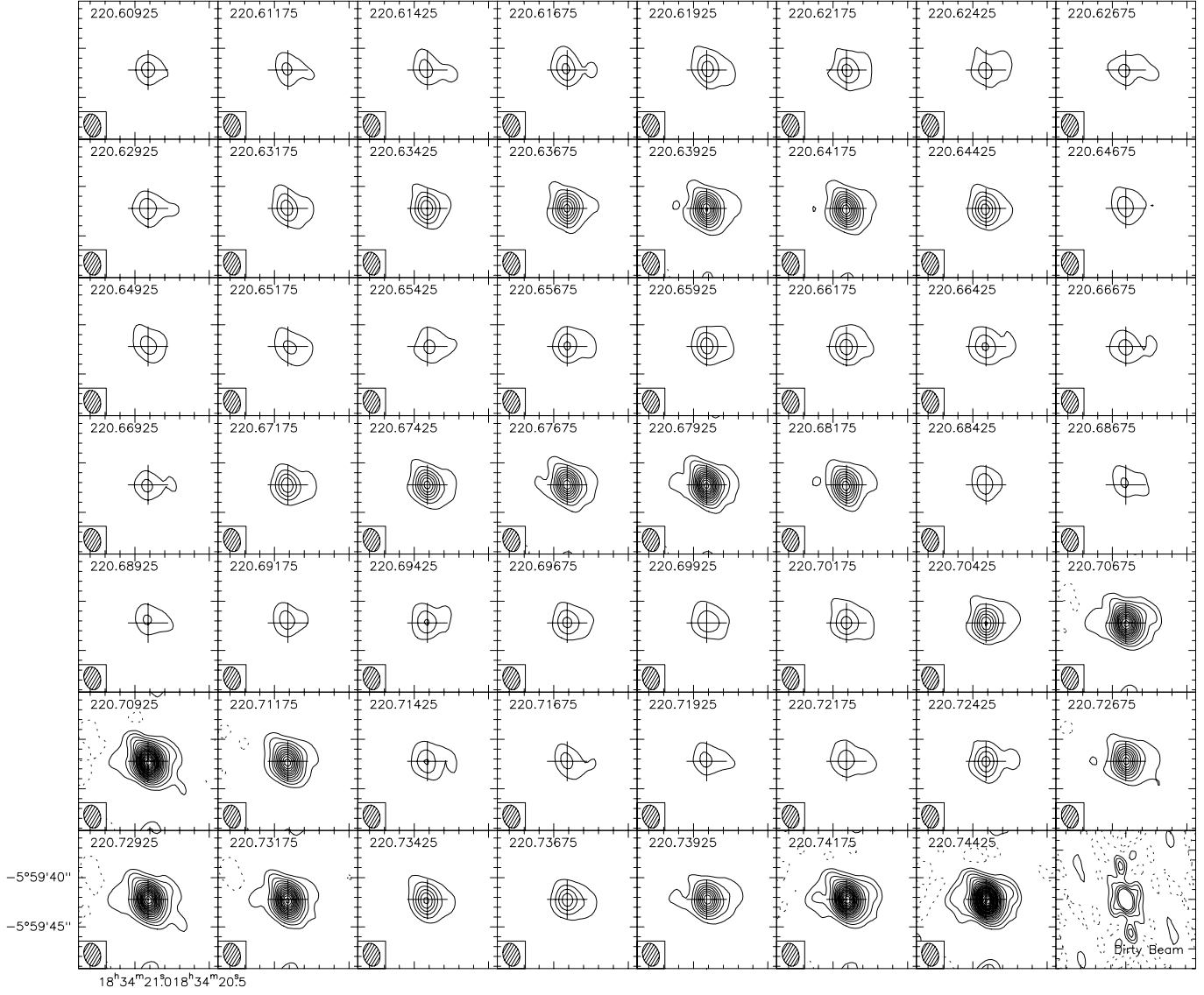


Fig. 5b. Same as **a**, in the $\text{CH}_3\text{CN } 12 \rightarrow 11$ transitions. The lowest contour levels and the increment are 40 mJy/beam. The dirty beam resulting from the observations and the clean beam ($2.37'' \times 1.66''$ respectively) are displayed. The frequency is indicated in the top left. This molecule emits from a very compact region near the star. A fit in the uv plane allows us to estimate the source size to be of about $1.2''$, which is assumed in the line analysis

However, this additional complication allows us to derive the source size from the observation of the same molecular transitions at the centre position used before and after the interferometric observations. This is the case for the $5 \rightarrow 4$ methanol transitions around 241 GHz.

Indeed, the observed antenna temperature of a Gaussian shaped emitting region as seen with a Gaussian beam, pointing at an offset position given by Δx and Δy from the source centre, is proportional to:

$$\int_{-\infty}^{+\infty} \exp\left(-\frac{x^2+y^2}{\alpha_B}\right) \times \exp\left(-\frac{(x+\Delta x)^2+(y+\Delta y)^2}{\alpha_S}\right) dx dy$$

$$= \exp\left(-\frac{\Delta x^2 + \Delta y^2}{\alpha_S}\right) \times \int_{-\infty}^{+\infty} \exp\left(-\left(\mu x^2 + \frac{2x\Delta x}{\alpha_S}\right)\right) dx$$

$$\times \int_{-\infty}^{+\infty} \exp\left(-\left(\mu y^2 + \frac{2y\Delta y}{\alpha_S}\right)\right) dy$$

$$= \frac{\pi}{\mu} \exp\left(-\frac{\Delta x^2 + \Delta y^2}{\alpha_S}\right) \times \exp\left(\frac{\Delta x^2 + \Delta y^2}{(\mu\alpha_S)^2}\right)$$

$$\text{with } \alpha_B = \frac{\theta_{\text{BEAM}}^2}{4 \times \ln(2)}, \alpha_S = \frac{\theta_{\text{SOURCE}}^2}{4 \times \ln(2)} \text{ and } \mu = \frac{\alpha_B + \alpha_S}{\alpha_B \alpha_S}.$$

The ratio of the observed integrated temperature of a given line at the source centre and at an offset from the centre is simply given by the ratio of $\frac{\pi}{\mu}$ and the above equation. Conversely, the source size θ_{SOURCE} can be estimated given observed intensity values. Of course, this analysis can not be done when $\theta_{\text{SOURCE}} \gg \theta_{\text{BEAM}}$ in which case the ratio equals one whatever the offset.

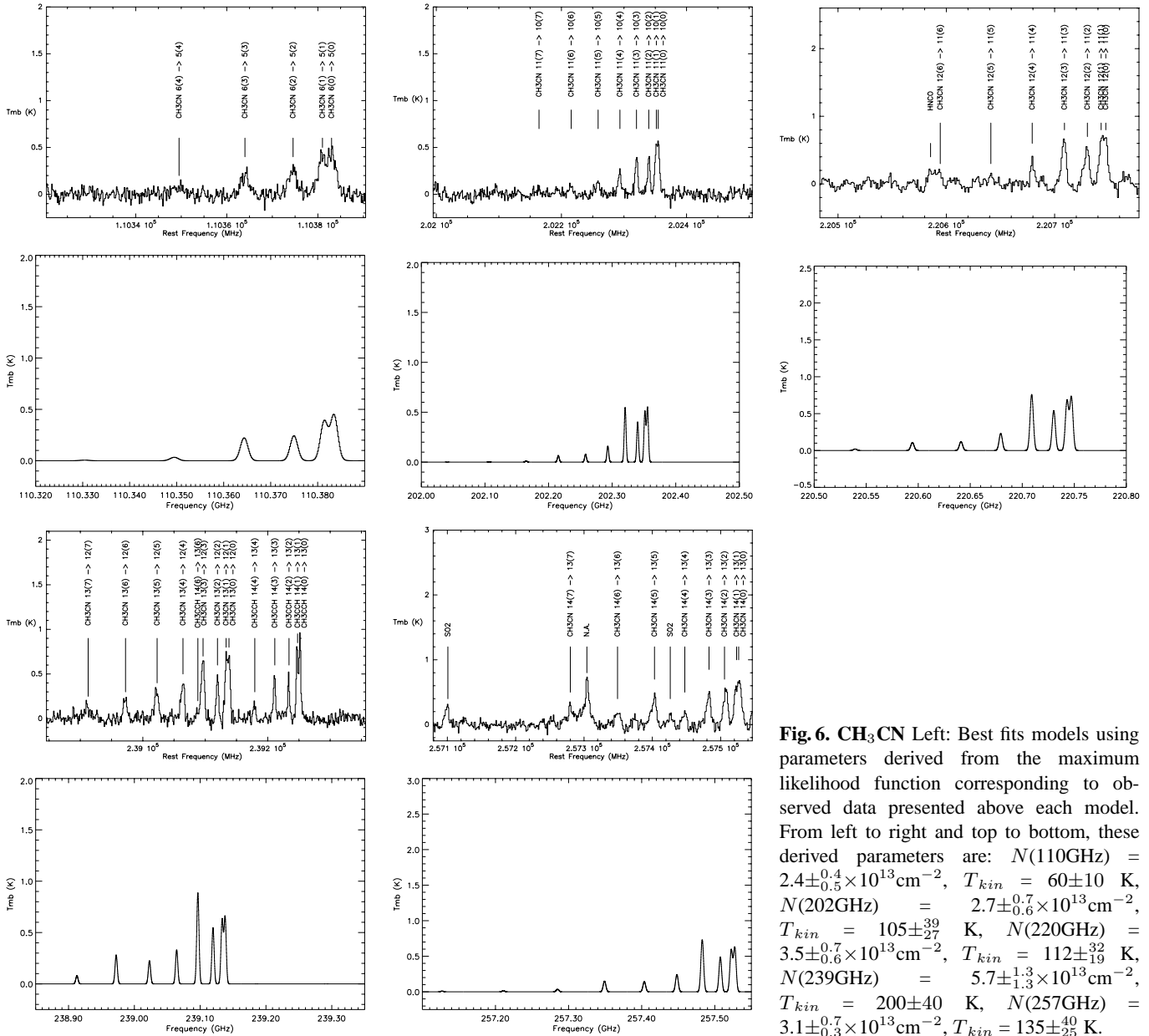


Fig. 6. CH₃CN Left: Best fits models using parameters derived from the maximum likelihood function corresponding to observed data presented above each model. From left to right and top to bottom, these derived parameters are: $N(110\text{GHz}) = 2.4 \pm_{0.5}^{0.4} \times 10^{13} \text{cm}^{-2}$, $T_{kin} = 60 \pm 10 \text{K}$, $N(202\text{GHz}) = 2.7 \pm_{0.6}^{0.7} \times 10^{13} \text{cm}^{-2}$, $T_{kin} = 105 \pm_{27}^{39} \text{K}$, $N(220\text{GHz}) = 3.5 \pm_{0.6}^{0.7} \times 10^{13} \text{cm}^{-2}$, $T_{kin} = 112 \pm_{19}^{32} \text{K}$, $N(239\text{GHz}) = 5.7 \pm_{1.3}^{1.3} \times 10^{13} \text{cm}^{-2}$, $T_{kin} = 200 \pm 40 \text{K}$, $N(257\text{GHz}) = 3.1 \pm_{0.3}^{0.7} \times 10^{13} \text{cm}^{-2}$, $T_{kin} = 135 \pm_{25}^{40} \text{K}$.

We benefitted from this in the case of the 241 GHz (5→4) methanol lines. We calculated the expected line ratio knowing the offset from the true position was 3'' in the first run of observations. The observed (241 GHz) methanol transitions before and after centre correction are shown in the Fig. 9. The source size can then be derived from the comparison of the two spectra, assuming the relative calibration is reliable. Including a 30% relative calibration uncertainty we are able to say the methanol emitting region size is about 8'' wide.

The three molecules (CH₃CN, CH₃CCH and CH₃OH) are associated with the presence of a hot core. However, the CH₃CN transitions are emitted from a compact region surrounding the central star and is probably directly created in a hot core chemistry (following or not grain evaporation). The methyl acetylene molecule, followed by the methanol molecule seem to pertain to

an intermediate region between the hot core region and a more quiescent region.

This last molecule (CH₃OH) must be a direct product of the grain evaporation as its abundance in the solid phase (Dartois et al. 1999) in this object is more than two orders of magnitude higher than in the gas phase.

The lower excitation temperature of the methanol molecule as compared to the high temperature of both methyl cyanide and propyne molecules supports the view that methanol lies in an intermediate region between the “pure” hot core and the halo surrounding it.

Indeed, given the high densities, we do expect the methanol to be globally thermalised.

Other authors have surveyed the molecular line emission of these molecules toward HII regions (Hatchell et al. 1998). In

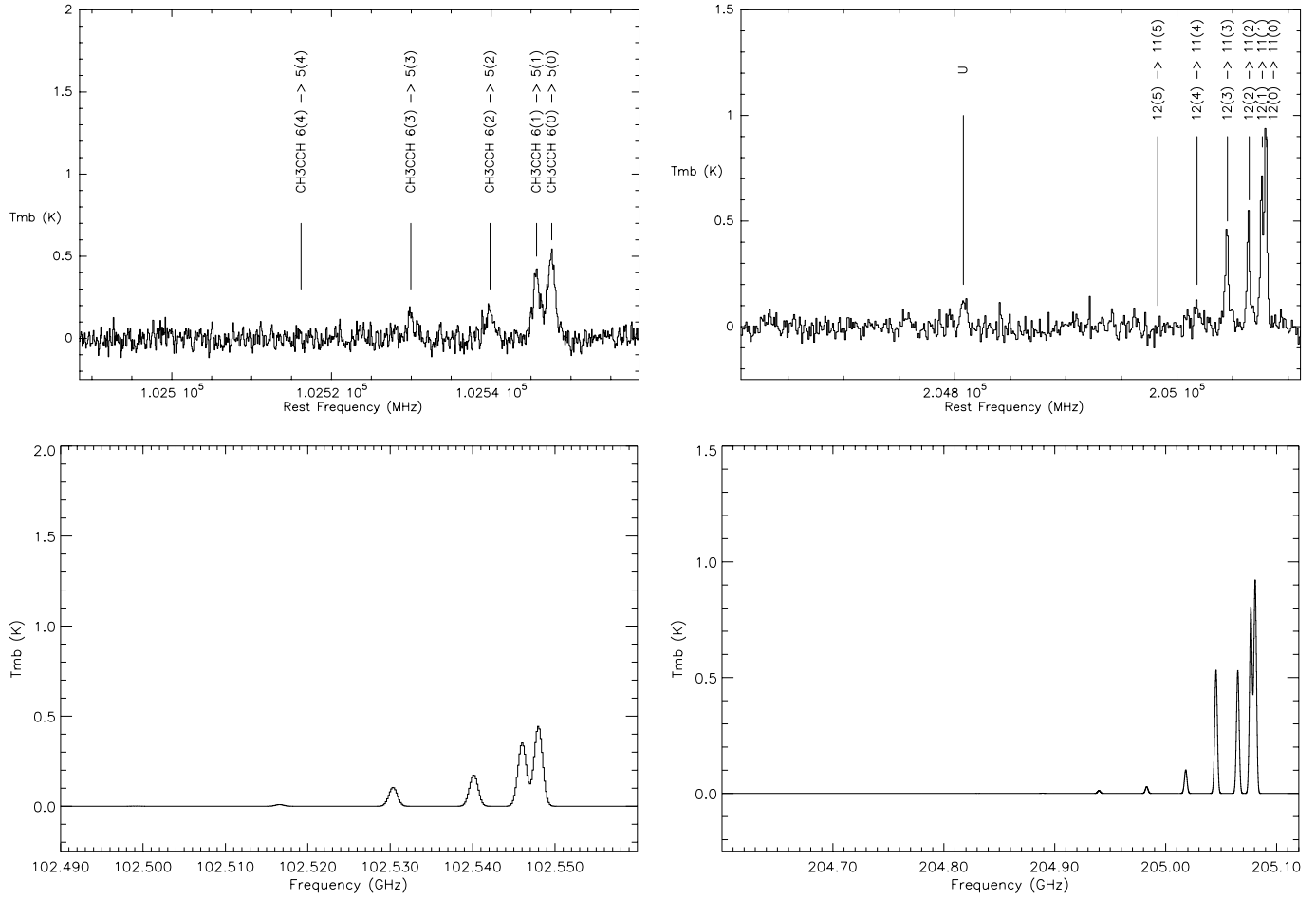


Fig. 7. Observations and corresponding best models spectra of the propyne molecule toward RAFGL7009S. $N_{CH_3C_2H}(102GHz)=2.7\pm_{0.7}^{0.9}\times 10^{14}cm^{-2}$, $T_{kin}=35\pm_{10}^7$ K. $N_{CH_3C_2H}(205GHz)=6.2\pm_{0.5}\times 10^{14}cm^{-2}$, $T_{kin}=55\pm_{10}$ K.

their sample, the source size is larger in methanol than in methyl cyanide, leading to the same conclusion. Thus methanol seems to be a very powerful molecule to follow grain evaporation or equivalently to trace the interface volume between a hot core and the cooler surrounding region.

5. Deuterated species

We have searched in this source for the deuterated species CH_3OD , HDO and $HDCO$ molecules at millimetre wavelengths. HDO and $HDCO$ molecules appeared readily whereas for CH_3OD , only a few lines are tentatively detected. We do not discuss the $HDCO$ observations as we cannot infer the D/H ratio based on the H_2CO lines which present a self reversed saturated absorption profile. To perform a comparison with the solid phase fractionation, we have used the infrared spectra provided both by ISO and UKIRT, and put constraints on the abundance of the OD containing species based on laboratory measurements.

5.1. HDO , H_2O and CH_3OD in the gas phase

High signal to noise data obtained with ISO in the $6\ \mu m$ wavelength range allow us to trace a hot gas phase water component

in addition to the cold saturated one already reported (Dartois et al. 1998). This component is much less abundant than the cold one, as suggested by Dartois et al. (1998) where it was reported to be at least a factor of three lower in abundance. The derived parameters for the hot H_2O are $4\pm_{0.15}\times 10^{17}cm^{-2}$ as shown in the Fig. 10, with a mean derived excitation temperature of $200\pm_{80}$ K.

With the IRAM 30m telescope we measured four HDO lines, presented in Fig. 11. We could then estimate the column density, source size and excitation temperature for this molecule using our maximum likelihood minimisation. The source size is $11''$, the column density $N_{HDO}=1.0\pm_{0.4}\times 10^{15}cm^{-2}$ and excitation temperature $180\pm_{50}^{70}$ K. For comparison, the corresponding rotational diagram is also presented in the same figure.

Using the information obtained from these observations, and comparing with the corresponding H_2O abundances for the same hot component (they should be spatially correlated), the derived $(D/H)_{HDO}^{gas}$ ratio for gas phase water is then of $2.5\pm_{1.3}^{2.1}\times 10^{-3}$. As the derived temperature is high, we think the source size is overestimated for this molecule, as it is very hard to keep a so huge volume of hot gas phase water. We therefore estimate the above D/H ratio value to be an upper limit.

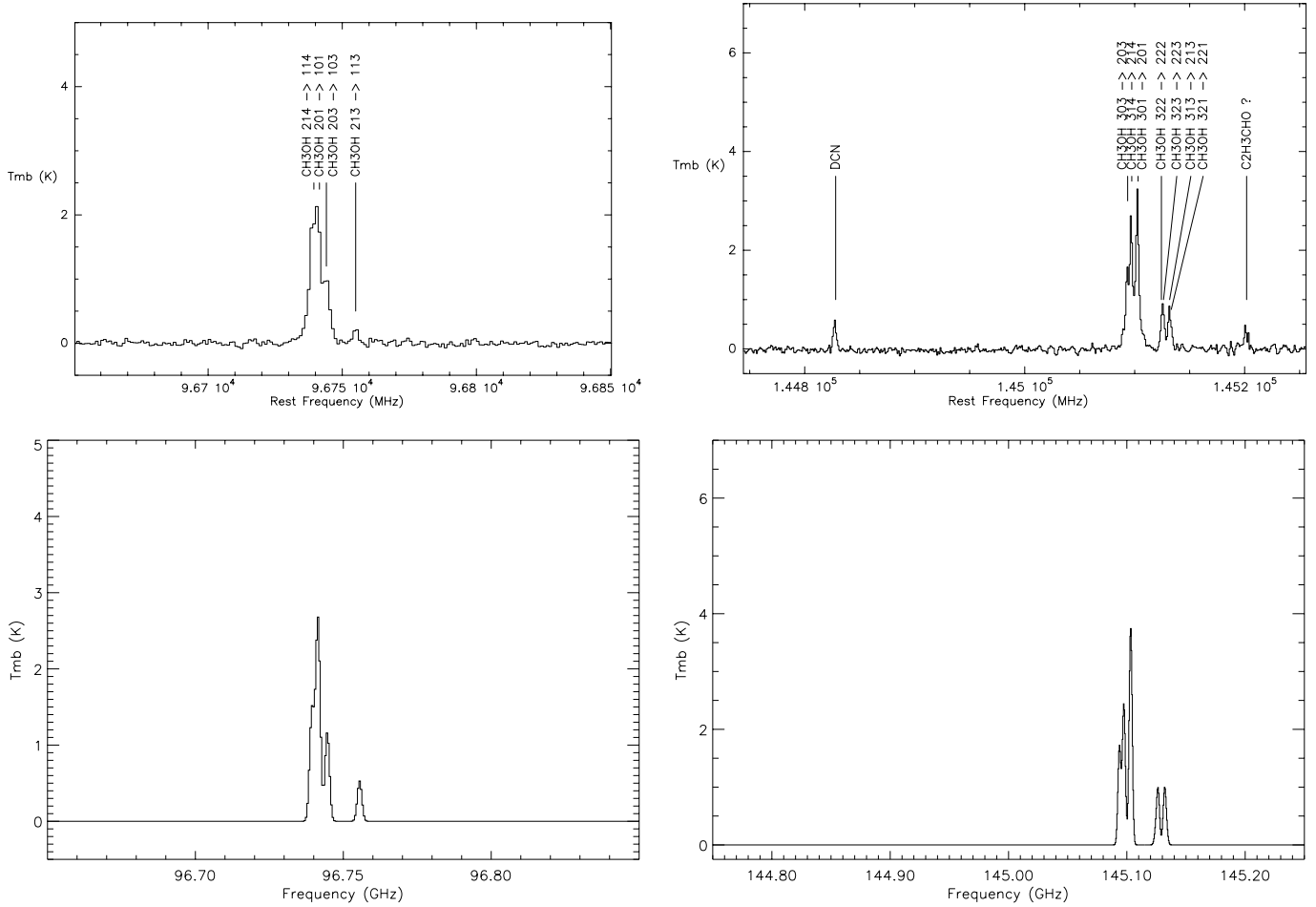


Fig. 8. Observations and corresponding best fit model spectra of the methanol molecule towards RAFGL7009S. $N_{\text{CH}_3\text{OH}}(96\text{GHz})=1.9\pm_{0.9}^{1.7}\times 10^{15}\text{cm}^{-2}$, $T_{\text{kin}}=15\pm_{5}^{12}\text{K}$. $N_{\text{CH}_3\text{OH}}(145\text{GHz})=2.0\pm_{0.2}^{0.3}\times 10^{15}\text{cm}^{-2}$, $T_{\text{kin}}=15\pm_{3}^{7}\text{K}$.

To pursue our investigation on deuterated species in this source, we also observed several CH_3OD rotational lines with the 30m telescope. The result of these observations are shown in Fig. 12. We detected the 1(1)-1(0)E (110188.860 MHz), 2(1)-2(0)E (110262.640 MHz) and 5(0)-4(0)A (226538.674 MHz) lines. In the individual plots of Fig. 12, we draw vertical lines to indicate the expected position for the CH_3OD lines, as well as the energy in cm^{-1} at which lies the upper level of the transitions. We thus only see low energy level lines.

Based on our minimisation analysis, the lines lying in the 3mm atmospheric window lead to a rotational temperature of $7\pm_{2}^{4}\text{K}$, a column density of $6\pm_{4}^{3}\times 10^{13}\text{cm}^{-2}$ in a source size of $\theta=8\pm 5''$.

In the 1 mm window, we find a temperature of $25\pm_{10}^{20}\text{K}$ and a column density of $1\pm 0.6\times 10^{14}\text{cm}^{-2}$. Taking into account these measurements and their associated uncertainties, we then derive $N=0.3\text{-}1.6\times 10^{14}\text{cm}^{-2}$ and $T=5\text{-}45\text{K}$.

For the methanol molecule, taking into account that the source size was estimated to be $\theta=8\pm 5''$ at 241 GHz, we obtain for the main isotope species a corrected column density of $1.2\pm 0.3\times 10^{16}\text{cm}^{-2}$ (different from that shown in the Fig. 8 where no source size has been specified).

The derived $(\text{D}/\text{H})_{\text{CH}_3\text{OD}}^{\text{gas}}$ ratio is then estimated to be between 10^{-2} and 2×10^{-3} .

5.2. Solid phase HDO

To compare the gas phase D/H ratio to that in the solid phase, we observed the OD stretching mode in the infrared spectrum obtained both by ISO and UKIRT in the vibrational associated wavelength range. We also determined in the laboratory the absorption cross section of this mode.

5.2.1. Laboratory experiments

Since the HDO molecule is rather unstable towards substitution, we decided to produce it *in-situ* in a controlled experiment in order to derive a reliable integrated absorption cross section of the OD stretching mode. Similar setups have been used successfully to obtain infrared spectra which are directly comparable to astronomical spectra (d'Hendecourt et al. 1996). The setup used to simulate interstellar spectra has been described elsewhere (Allamandola 1987). It consists of a liquid helium flow cryostat cooled to temperatures of 4K-300K, and a CsI window

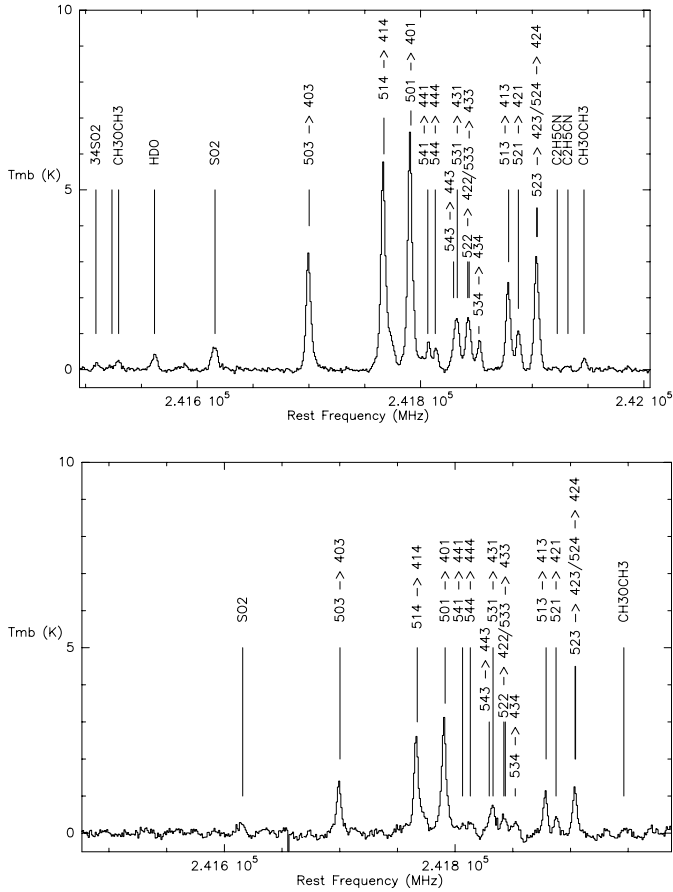


Fig. 9. Observed methanol 5→4 transitions at the centre of the ultra compact HII region (upper panel) and at a North-East offset of 3'' (lower panel). The difference in intensity allows to estimate the methanol source size (see text). $N_{CH_3OH}(241GHz \text{ upper panel}) = 3.8 \pm_{0.5}^{0.6} \times 10^{15} \text{ cm}^{-2}$, $T_{kin} = 21 \pm_4^5 \text{ K}$. $N_{CH_3OH}(241GHz \text{ lower panel}) = 1.6 \pm_{0.3}^{0.3} \times 10^{15} \text{ cm}^{-2}$, $T_{kin} = 18 \pm_6^7 \text{ K}$.

onto which our gas mixtures are slowly condensed. Mixtures are prepared separately in an adjoining stainless steel vacuum line. Condensed mixtures may be UV irradiated using a microwave discharge H_2 lamp. The cryostat is coupled to an FTS infrared spectrometer (Bruker IFS 66v). Spectra presented here were recorded at a resolution of 1 cm^{-1} , comparable to the ISO SWS resolution. We have performed two different experiments. The first involved deuterated methane and oxygen, and was aimed at determining the integrated absorption cross-section of the OD stretch. The second, based on water ice mixed with molecular deuterium, was used to directly compare with astronomical spectra.

5.2.2. Determination of the OD stretch absorption cross-section

We have condensed a mixture of deuterated methane (CH_3D) mixed with an equal proportion of O_2 at 10K. After UV irradiation with the microwave H_2 discharge lamp that produces hard UV photons (Okabe 1980), we principally formed H_2O , HDO,

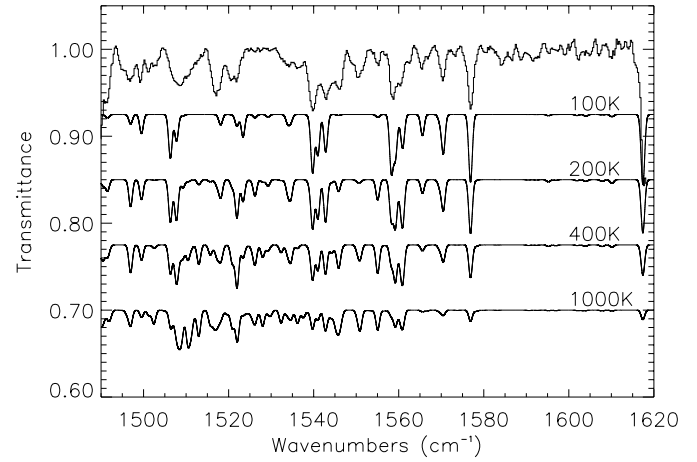


Fig. 10. H_2O ro-vibrational lines from the hot component seen in absorption with ISO towards RAFGL7009S. Modelled spectra at different temperatures are shown for comparison, assuming the same Doppler parameter as the one used in Dartois et al. (1998). We derive $N_{HDO} = 4 \pm_{0.15} \times 10^{17} \text{ cm}^{-2}$ and a mean temperature of $150 \pm 70 \text{ K}$.

CO and CO_2 as can be seen in the vibrational spectrum presented in Fig. 13. On this figure the upper curve is the spectrum of the condensed mixture ($CH_3D:O_2=1:1$) before irradiation, where the observed lines are all attributed to transitions arising from the CH and CD in CH_3D . The lower curve is the resultant spectrum after photolysis. The assignments of the vibrations are indicated below the curve. H_2O and HDO are identified via their OH and OD stretch at around 3300 cm^{-1} and 2450 cm^{-1} , as the mass difference between D relative to H induces a shift of the OH stretching mode such that $\bar{\nu}_{OD} \approx \bar{\nu}_{OH}/\sqrt{2}$. HDO is then responsible for the transition observed around 2450 cm^{-1} . Note that the OH stretch pertains both to H_2O and HDO and is indistinguishable in the broad amorphous band observed around 3300 cm^{-1} . Finally, the broad nature of the two observed bands, due to hydrogen bonding of the clustered molecules, ensures that the clusters are themselves amorphous. This is essential to determine the integrated absorption cross-section to be used in the comparison with astronomical data.

To a first approximation, we assume in the photolysis process that the formation rate of H_2O , HDO and D_2O is ruled by the statistics of the D/H ratio from the deuterated methane molecule. We can then proceed to evaluate the oscillator strength for the OD stretching mode in the laboratory spectra. Let us denote by r the initial isotopic ratio in deuterated methane:

$$r = \frac{n_H}{n_H + n_D} = \frac{3}{4}.$$

During photolysis, we then produce $r^2 H_2O$ molecules, $2r(1-r)$ HDO and $(1-r)^2 D_2O$ (9:6:1). If we write the integrated absorbance ratio observed for the OH and OD stretching modes we then obtain, regardless of the molecules from which they are part of:

$$\frac{\int \tau_{OH} d\bar{\nu}}{A_{OH} \times f_{OH}} = \frac{\int \tau_{OD} d\bar{\nu}}{A_{OD} \times f_{OD}}$$

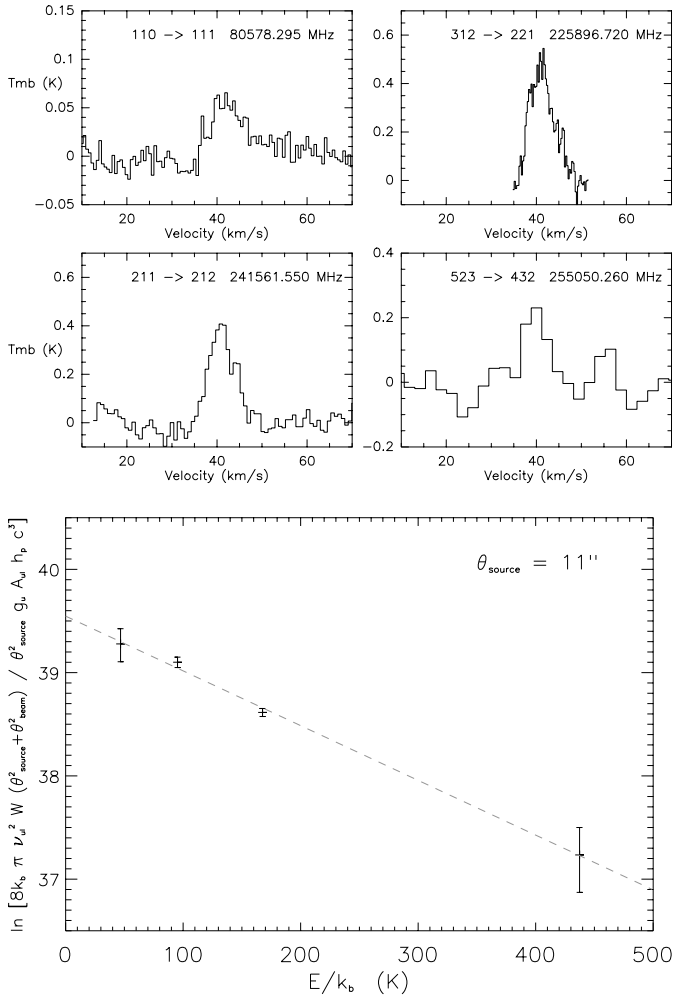


Fig. 11. HDO $1_{10} \rightarrow 1_{11}$, $3_{12} \rightarrow 2_{21}$, $2_{11} \rightarrow 2_{12}$ and $5_{23} \rightarrow 4_{32}$ transitions. The best fit rotational diagram was obtained with a FWHM source size of $11''$ leading to a column density of $N_{HDO} = 1. \pm 0.4 \times 10^{15} \text{ cm}^{-2}$ with an excitation temperature of $180 \pm_{50}^{70} \text{ K}$.

where f_{OH} and f_{OD} are the number of OH and OD groups participating in the respective features, A_{OH} and A_{OD} are the integrated absorption cross-sections. Remembering that $A_{OH} = A_{H_2O}/2$, we deduce:

$$A_{OD} = \frac{\int \tau_{OD} d\nu}{\int \tau_{OH} d\nu} \times 3 \times \frac{A_{H_2O}}{2}.$$

Measurements of the integrated absorbances in the spectrum after the photolysis lead us to:

$$A_{OD} = \frac{5.68 \pm 0.25}{47.54 \pm 0.75} \times 3 \times \frac{2. \times 10^{-16}}{2} \\ \sim 3.6 \pm 0.2 \times 10^{-17} \text{ cm.molec}^{-1}.$$

The half width at half maximum of the OD stretching line in the amorphous state measured in this spectrum is about 170 cm^{-1} . The optical depth at the line centre can be approximated by:

$$\tau_{\nu 0} \approx \frac{N_{HDO} \times A_{OD}}{\Delta\nu} \approx N_{HDO} \times 2.1 \times 10^{-19} \text{ molec.cm}^{-2}.$$

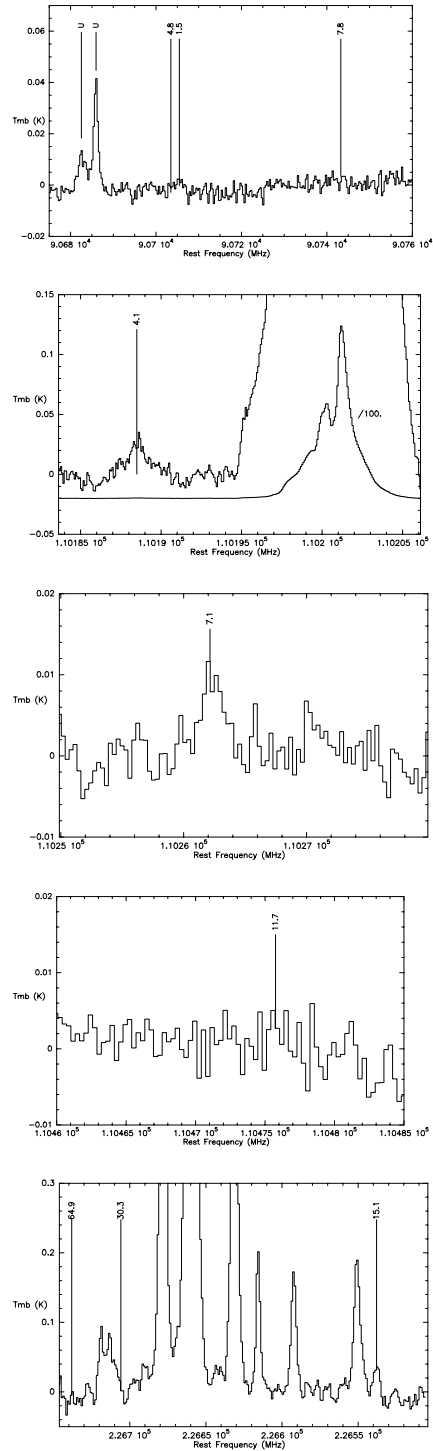


Fig. 12. CH₃OD lines observed toward RAFGL7009S. The expected lines positions are indicated as well as the corresponding upper state energy (in cm^{-1}) of the transition.

For astronomical purposes, this number implies that with a signal-to-noise ratio of 30, one can determine with a 3σ accuracy an optical depth $\tau_{\nu 0}$ of 0.1 corresponding to a column density of $4.7 \times 10^{17} \text{ cm}^{-2}$.

We emphasise that the line centre absorption cross-section will change when one goes to the crystalline form of water

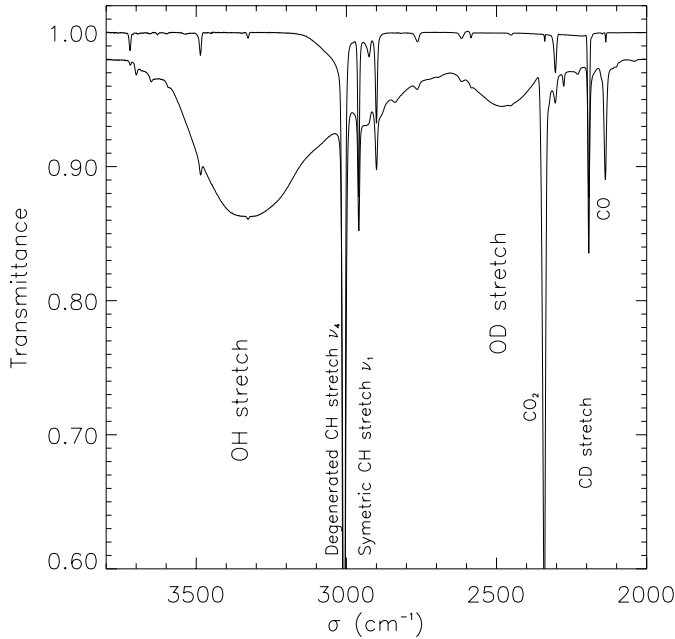


Fig. 13. Spectra of a $\text{CH}_3\text{D}:\text{O}_2$ —1:1 ice mixture which were condensed at 10K (top curve), and after irradiation by UV photons (lower curve). The irradiation mainly produces H_2O as well as HDO and D_2O , giving rise to the two broad bands around 3300 cm^{-1} and 2500 cm^{-1} . The different vibrational modes observed are labelled.

ice. In this case, the line will be sharper as shown in the next experiment, rendering a tentative detection easier.

5.3. Production of an H_2O — HDO mixture

This first experiment was dedicated to the evaluation of the integrated absorption cross section of the OD stretching mode in HDO . We can now move onto the interpretation of the astronomical spectra using a more realistic mantle composition i.e. a water dominated one.

As is well known, astronomical ices are largely dominated by water ice. We have chosen to obtain a pure H_2O environment in which the minor species HDO is embedded. We have thus condensed a mixture of H_2O and deuterated molecular deuterium (D_2) at 10K that was irradiated using the same UV lamp discussed above. We then converted part of the H_2O molecules into HDO . After slight warming, the extremely volatile D_2 , HD and H_2 molecules that were present or created in the process, migrated into the ice matrix and escaped the sample. Thus we ended up with a mixture essentially containing H_2O , HDO and D_2O , the latter being much less abundant.

We discuss the experimental results together with the astronomical comparison hereafter.

We have obtained spectra of RAFGL7009S with both the ISO satellite (SWS01 template) and the United Kingdom InfraRed Telescope (UKIRT). The ISO spectrum gives a view of the complete spectrum of the source (d’Hendecourt et al. 1996). The ground based observations are much more sensitive in the atmospheric windows. Unfortunately, with the UKIRT CGS4,

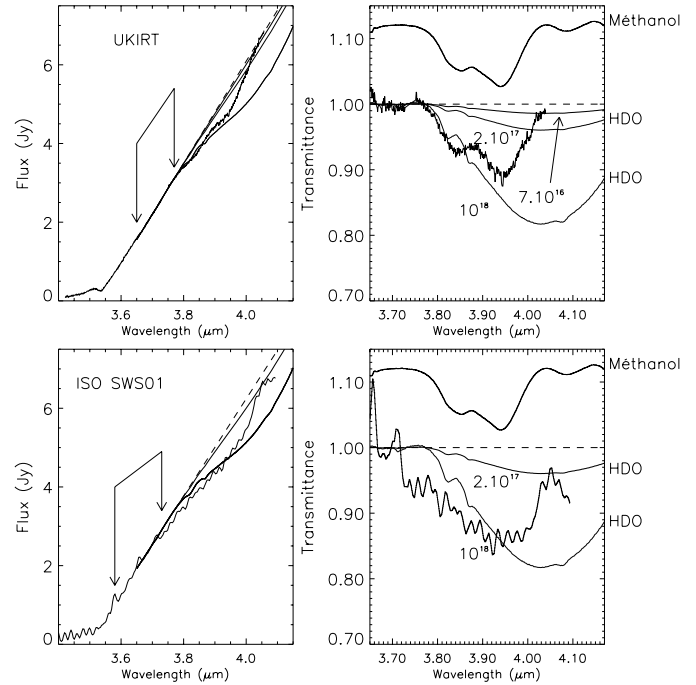


Fig. 14. estimate of an upper limit on the solid HDO content of the ice towards RAFGL7009S using ISO and UKIRT spectra. See text

we have only measured the spectrum region located just before the strong telluric CO_2 absorption, between 3.4 and $4.04\text{ }\mu\text{m}$. With the ISO satellite, we only used the part of the spectrum in the “1e” band (from 3.4 to $4.1\text{ }\mu\text{m}$), as the next band (“2a”) is less sensitive and also because in this band the spectral response possesses a large feature peaking at $4.1\text{ }\mu\text{m}$. This feature could appear as an absorption band if badly subtracted, which would result in a spurious identification of a weak band. It is more secure to use the “1e” band as it covers half of the expected amorphous HDO absorption feature.

The main result from the UKIRT observation has been described extensively in Dartois et al. (1999). It consisted in the detection of various vibrational modes of CH_3OH that are particularly well matched through laboratory simulations and allowed us to confirm the high abundance of this molecule in the mantles toward this object. We present in Fig. 14 the continuum estimate (left panel) and the resultant baseline corrected spectrum (right panel) between 3.4 and $4.04\text{ }\mu\text{m}$ for the UKIRT spectrum, $4.1\text{ }\mu\text{m}$ for the ISO spectrum. Both spectra clearly show a double methanol feature attributed to combination modes. As we are looking for a large feature ($\text{FWHM} \sim 0.2\text{ }\mu\text{m}$ at $\sim 4\text{ }\mu\text{m}$), we fitted the continuum with a first order polynomial, whose slope was derived by adjusting the data in the range shown by the arrows. We chose a first order polynomial to be sure not to introduce any artificial curvature as could be the case with higher orders. The continuum is expected to curve downwards in this range since the $3\nu_{\text{vibration}}$ mode of the water ice band will absorb there. This assumption can be safely verified in the numerous ice dominated spectra recorded by ISO and especially the ones where an HDO detection was reported by Teixeira et

al. (1999). On the right part of the figure, we display the transmittance spectra after subtraction of the polynomial. We have normalised the laboratory HDO spectra shown in Fig. 13 in accordance to the derived integrated absorption cross-section for the OD stretching mode. We display the transmittances expected for various column densities, as indicated on the curves in the Fig. 14. We do not detect the amorphous HDO absorption band, the smaller value being our estimate on the upper limit. The upper curve represents the methanol contribution to the astronomical spectrum (see Dartois et al. 1999 for a more detailed discussion).

The HDO column density is estimated to be less than $7 \times 10^{16} \text{ cm}^{-2}$. Using the H_2O column density in this source ($\sim 1.2 \times 10^{19} \text{ cm}^{-2}$, d'Hendecourt et al. 1996) the $(\text{D}/\text{H})_{\text{HDO}}^{\text{ice}}$ ratio is then $\leq 6 \times 10^{-3}$.

Contrary to gas phase millimetre wave spectra, which are linked to the rotational excitation ladder of the molecules, we probe in the infrared the vibrations of molecules. In the solid phase, the complex rovibrational spectrum merges into a broad main feature whose position will be less specific for the particular molecule involved but sensitive to the kind of atomic bonds. This implies that every molecule possessing an OD bond (such as HDO, CH_3OD , $\text{C}_2\text{H}_5\text{OD}$...) will absorb in the same region. This behaviour is crucial as it strengthens the derived upper limit which holds very strictly for HDO as well as for CH_3OD . On the basis of the high CH_3OH abundance detected in RAFGL7009S (Dartois et al. 1999) and assuming the integrated absorption cross section ratio of OH groups are conserved when one substitutes hydrogen by deuterium, we can determine an upper limit on the D/H ratio in methanol, given by:

$$(\text{D}/\text{H})_{\text{CH}_3\text{OD}} \leq \frac{2 \times 10^{-16} \times N_{\text{H}_2\text{O}} \times (\text{D}/\text{H})_{\text{HDO}}}{1.3 \times 10^{-16} \times N_{\text{CH}_3\text{OH}}}$$

which leads to: $(\text{D}/\text{H})_{\text{CH}_3\text{OD}}^{\text{ice}} \leq 3 \times 10^{-2}$.

5.4. Discussion

5.4.1. Solid phase

In a paper on the surface chemistry of deuterated molecules, Tielens (1983) calculates the D/H ratio expected in grain mantles. The main point addressed by surface chemistry is that whereas in the gas phase the D/H ratio in HD and to a lesser extend in D (atomic deuterium) should approach the cosmological value, it will be different on grain surfaces. Indeed, the change in mass between D and H atoms by a factor of 2 considerably influence the behaviour of the species relative to their surface binding energy. The residence time-scale on grains will therefore favour deuterated species over hydrogenated ones. This aspect as well as the difference in activation barriers for the reactions involving deuterated species was treated by Tielens (1983).

The numbers derived in his model are very high. In Fig. 1b of his paper are plotted the expected $(\text{D}/\text{H})^{\text{ice}}$ ratios of the most abundant deuterated molecules relative to their hydrogenated counterparts in the mantle as a function of hydrogen number density. The deuterium enrichment increases steeply with den-

sity. In the source we study here, the mean density is evaluated to be about 10^6 cm^{-3} . Using these numbers we can exclude the very high enrichment derived from the model of Tielens, which would lead to D/H ratios > 1 , orders of magnitude above the upper limit we measure.

The D/H ratio in ices seems not abnormally high, if compared to the gas, as our upper limits lie just above the ratio measured in the gas for HDO and even slightly lower if we compare to IRAS16293-2422 (van Dishoeck et al. 1995). This implies that the D/H ratio, if lying just below the limits given in this study, stays almost constant in the gas after mantle evaporation.

Teixeira et al. (1999) recently reported the detection of HDO in ices toward massive young stars. Following their discussion, it remains unclear if it provides support for the assumption that the origin of high levels of deuterium fractionation in hot cores is evaporation of the deuterated species from grain mantles. Indeed, these observations can not distinguish between fractionation generated by low temperature gas phase chemistry, followed by accretion onto dust, from the production of deuteration in or on grain surfaces.

In particular, some points need to be investigated in the future if the fractionation is attributed to grain chemistry. Why should a source like W33 A, the one with the highest extinction and with the coldest grains, displays a $(\text{D}/\text{H})_{\text{H}_2\text{O}}^{\text{ice}}$ ratio more than ten times lower than NGC 7538 IRS9, whereas the former appears colder and display stronger ice absorptions?

There is an indication of the evolution of NGC 7538 IRS9 compared to W 33A that shows the latter is cooler. It is given by the shape of the $15.2 \mu\text{m}$ CO_2 bending mode which possess a triple peak structure in W 33A whereas it shows a double peak substructure in NGC 7538 IRS9. This structure is associated with a molecular complex formation in the ice (Dartois et al. 1999) and the evolution of the substructure traces the temperature evolution of the ices, showing W33A is apparently colder. The same temperature evolution behaviour is found by Boogert et al. (2000) using the $^{13}\text{CO}_2$ stretching mode, as well as the flux ratio at 45 and $100 \mu\text{m}$. What can then explain a so huge difference between the two sources given they share the same bolometric luminosity (9.2×10^4 for NGC7538 IRS9; 1.1×10^5 for W 33A, see reference in Boogert et al. 1999)?

5.4.2. Gas-solid phase models

Recently, Bergin et al. (1998) have also discussed an alternative to classical grain surface chemistry through the formation of ices behind shock waves. They show in this model a plot of the resulting relative concentration of $\text{HDO}/\text{H}_2\text{O}$ in the grains versus that of $\text{CO}_2/\text{H}_2\text{O}$. In this diagram, a box is drawn and said to represent the observed values in the ISM. To draw this box, the authors are accepting the hypothesis that the gas phase measurements directly mimic the deuterium fractionation obtained on grain mantles, which still remains to be proven in the general case.

Another point to be addressed for a full discussion is the fact that all the models have been generated for dust temperatures strictly above 25K. Extrapolating from the curves presented in

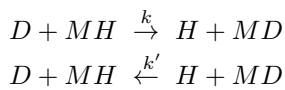
Fig. 2. to a 10K curve, a large fractionation is expected (above 10^{-2}). If the grains remain at a temperature above 25K, this model prevents a lot of deuterium fractionation. Indeed, the residence time-scale for D and HD is reduced by a huge factor as compared to a grain at 10K. The residence time-scale for a species on a grain is given by $\tau = \nu \exp(-E_B/kT)$, where ν is a characteristic vibration of the adsorbed species, where E_B is the binding energy to the surface, k the Boltzmann constant and T the grain temperature. For H and H_2 E_B/k is between 200 and 700K depending on which ice the molecule is adsorbed (Schmitt 1993). The corresponding ratio of residence time-scales at 25K and 10K is then so large that it deserves a complete discussion in gas-grain interacting models. As an example, Brown & Millar (1989), with $n_{H_2} = 3 \times 10^4 \text{ cm}^{-3}$ and grains at 10K, find a ratio HDO/ H_2O of 8.2×10^{-3} , well above the fractionation at 25K and with a sticking coefficient of only 0.3 for H and D atoms. Finally, the influence of higher gas densities such as the one met in RAFGL7009S ($n_{H_2} \approx 10^6 \text{ cm}^{-3}$) must also be investigated. It would be interesting to recalculate the same models with a density more appropriate to the source reported in this paper.

In the models by Tielens (1983) and Brown & Millar (1989) which both include surface chemistry involving deuterium, large fractionation is predicted for all grain species considered at densities greater than 10^4 cm^{-3} . If we believe that observations of high enrichment in deuterated species in hot core regions are the consequence of the evaporation of grain mantles, we would then expect from these models comparable fractionation for HDO, NH_2D and HDCO. In the Brown & Millar model, the result presented in their Table 2, shows that the $\frac{NH_2D}{NH_3} / \frac{HDO}{H_2O}$ ratio lies within the range 0.12-0.64. In the model of Tielens (1983) HDO, NH_2D and HDCO roughly exhibit the same deuterium enrichment. This is in contradiction with hot cores measurements giving $0.001 < HDO/H_2O < 0.004$ (Jacq et al. 1990), $NH_2D/NH_3 \sim 0.06$ and $HDCO/H_2CO \sim 0.14$ (Turner 1990). The inconsistency comes mainly from the fact that these ratios are not verified simultaneously, suggesting that different enrichment mechanisms apply to different species.

5.4.3. Pure gas phase

We also have to take into account the observations of high deuterium enrichment in radicals, molecular ions and molecules which never come directly from grain evaporation and are believed to result from pure gas phase reactions (Gerin et al. 1987; Guélin et al. 1982). However, these implied molecules possess formation routes that seem decoupled from the grain chemical evolution.

The equilibrium rate constant relating forward and backward reactions in the cases of pure D/H exchange like:



are classically related by:

$$K = \frac{k}{k'} = \frac{Q_{MH} Q_D}{Q_{MD} Q_H} \frac{\sigma_{MH}}{\sigma_{MD}} \exp(-E_0/kT)$$

where MH and MD are molecules, radicals or ions, Q is the partition function, which includes internal terms (electronic, vibrational, rotational) and translational terms. σ_{MH} and σ_{MD} are the symmetry numbers of each species included to take into account the symmetry statistic of each species. E_0 is the difference in vibrational zero point energies between the two species MH and MD. The multiplicative term is generally of the order of unity, whereas the exponential term is highly temperature dependent. Low temperature fractionation can sometimes then proceed simply because a key reaction will displace the equilibrium in the deuterium enrichment way. Thus apart from the formation reactions of the hydride and deuteride molecules by reactions involving other species (such as $CH_2D + O \rightarrow HDCO + H$), the exchange reaction favours deuteration at low temperature as the vibrational zero point energies are generally lowered due to the lower M-D vibration frequencies compared to the M-H.

Ion molecule chemistry such as the one implying H_2D^+ and CH_2D^+ play a major role in pure gas phase chemistry. Recently Shah & Wooten (1999) have measured NH_2D/NH_3 ratios towards low-mass star formation regions and argue that the high deuterium enrichment observed is compatible with pure ion-molecule chemistry, and that molecules observed in region of ices evaporation could in fact simply result from the reappartition in the gas of molecules enriched in the gas and subsequently depleted on grains without any further enrichment in the solid phase.

Recently, Roueff et al. (2000) reported the detection of doubly deuterated ammonia in the dense core of L134N at the level of 10% compared to singly deuterated ammonia and question whether it is possible to obtain such observed high D/H ratios with gas phase chemistry. Tiné et al. (2000) find that NH_2D/NH_3 high fractionation levels are compatible with a C and O depleted gas phase chemistry. As the species such as CO condense on grains, molecular ions are destroyed on longer timescales. In such a case, the gas phase fractionation can proceed efficiently as the abundance of ionised precursors is enhanced.

5.4.4. Summary

The observations of deuterated species presented above show that it is difficult to obtain a definite picture on the dominant route for fractionation (either low temperature gas phase chemistry or grain surface and bulk UV assisted chemistry).

In the observations presented here, the methanol molecule is orders of magnitude more abundant in the solid phase than in the gas phase. A very small evaporated fraction (1% to 0.1%) is sufficient to account for the methanol gas phase abundance observed. It suggests that the measured D/H enrichment for CH_3OH in the gas of at least a factor of 100 and perhaps a factor of 1000 above the cosmological D/H is indeed achieved by grain chemistry for this species.

These observations are not a definite proof that grains are responsible for the general enrichment in such sources but that it seems a good tracer of grain deuteration in lines of sight where it has been measured in the solid phase.

Finally we stress that a careful search for the CD stretching mode in the spectra of embedded objects is of high priority to put further constraints on the degree of deuteration of solid carbon species such as CH_3D , CH_2DOH and HDCO . Indeed the CD stretching mode for these molecules falls in the wavelength range 4.5-4.9 μm (see Fig. 13, this paper for CH_3D), a region accessible from ground based telescopes. Opportunities are opened by new generation telescopes such as the VLT and Gemini. As seen by the results presented here for HDO, we stress the necessity to obtain very high signal-to-noise ratio, up to 10^3 in order to detect CD or to obtain meaningful upper limits.

6. HCN and HNC

The HNC and HCN isomers represent a very interesting chemical probe in interstellar sources. These two molecules have similar dipole moments and their different intensities ratios therefore reflect chemical changes rather than excitation effects. The HCN to HNC abundance ratio present a strong chemical temperature dependence. In the OMC-1 region, this ratio has been shown to vary significantly in regions with different kinetic temperatures (Schilke et al. 1992), being of ~ 80 in Orion-KL and falling to 5 in cooler regions.

Recently, Hirota et al. (1998) have studied the HNC/HCN ratio in dark cloud cores and shown a clear temperature dependence of this ratio when comparing the available data on these molecules (see their Fig. 4).

When we observed the HCN(1-0) transitions (Fig. 15) we could see two strong self absorptions arising at different velocities. We could accurately determine these velocities thanks to the hyperfine structure, and found $43.0 \pm 0.2 \text{ km.s}^{-1}$ and $46.3 \pm 0.2 \text{ km.s}^{-1}$. The HCN(1-0) spectrum is very complicated but the absorption at 43.0 km.s^{-1} seems roughly a factor of two stronger than the one observed at 46.3 km.s^{-1} .

When one looks at the HNC(1-0) spectrum measured at the same position, it is also strongly self absorbed and present a T_{mb} of the same order of magnitude. However, there is only one emission and self absorption, both centred at 43.0 km.s^{-1} , and nothing at 46.3 km.s^{-1} (indicated by a vertical line in the Fig. 15).

Thus, although the spectra are too complicated to derive accurate numbers without observing the HC^{15}N , H^{13}CN and HN^{13}C isotopes, we clearly sample two different physical regions.

The difference in opacity between the 43 and 46 km.s^{-1} components is much more pronounced for HNC than for HCN. The most likely explanation is that the gas associated with the 46 km.s^{-1} feature is warmer than the gas associated with the 43 km.s^{-1} , hence has a larger HCN/HNC abundance ratio by roughly one order of magnitude. The 43 km.s^{-1} component is also seen in other species (HCO^+ , CS ,...). It is typical of fairly cold gas.

Owing to the temperature behaviour of the HNC/HCN ratio, as described in Hirota et al. (1998), we can conclude that with the 43.0 km.s^{-1} component we are probing a very cold phase ($T < 25 \text{ K}$), whereas the component at 46.3 km.s^{-1} must have

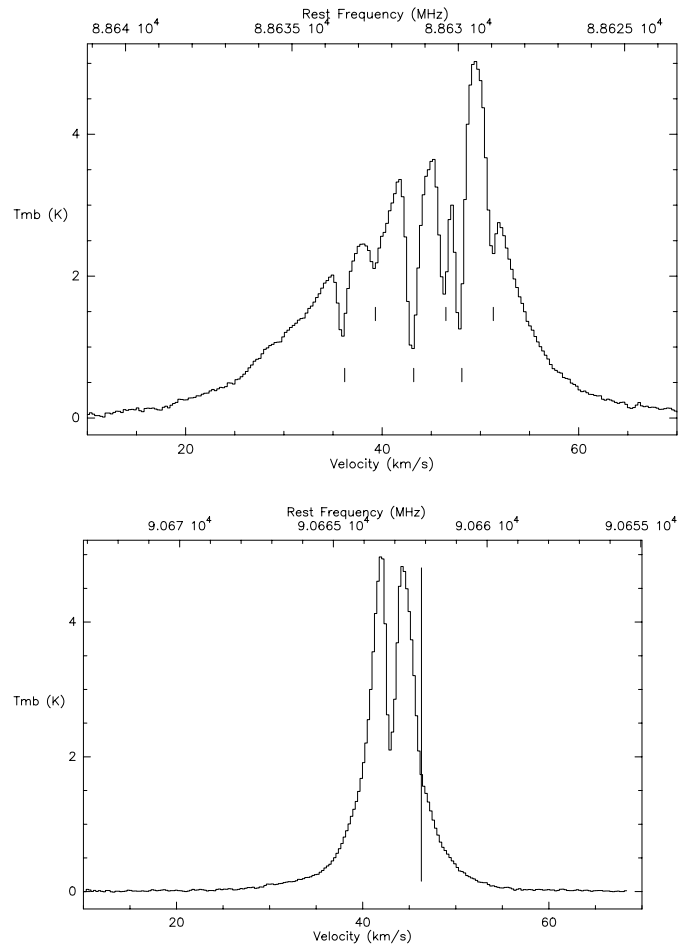


Fig. 15. HCN(1-0) (top) and HNC(1-0) (bottom) spectra observed toward RAFGL7009S. The velocity scale for HCN has been adjusted for the 1-0, $F=2-1$ transition at 88631.8473 MHz. HCN shows two strong triplet absorptions (indicated by the two sets of vertical tick lines) whereas only one absorption is seen for HNC. The vertical line in the HNC spectrum indicate the position where we would expect the emission of the second hyperfine component seen in absorption in the HCN spectrum.

been formed at temperatures above 40 K. The former is probably associated with the cold parts of the cloud (envelope) whereas the latter could trace the outflow observed in CO (Shepherd & Churchwell 1996). Indeed, a high HNC/HCN abundance ratio can be maintained in the gas phase if and only if both species have stayed in cold gas since their formation. A passage through a high temperature phase would remove the HNC isomer from the gas phase, and convert it to HCN. As we have observed for CS, the kinetic temperature of the 43.0 km.s^{-1} component is quite low, in the 10-50K range. For the other component, we have no constraint on its rotational excitation temperature. Maps of these two isomers (and their respective isotopes to avoid opacity effects), should permit us to probe and decipher the geometry of the cold envelope versus the outflow.

7. Conclusion

We have presented observations of the infrared source RAFGL7009S taken in the millimetre and infrared wavelength range, allowing the determination of global source parameters such as:

- the bolometric luminosity of the source corresponds to a late O or early B star.
- the envelope mass is dominated by a high fraction of cold dust (21.8 to 43.4M_⊙).
- the mean H₂ density is above 10⁶cm⁻³ at the 10'' scale (~0.1 pc).

The observations of different gas phase molecules in the millimetre range allow to probe various spatial and chemical aspect of the envelope. We determine:

- the position of the compact HII region, as probed with the hot core molecule CH₃CN. It is accurately determined with interferometer observations at arcsecond scales.
- The difference in size of the source as seen with CH₃CN, CH₃C₂H and CH₃OH. The latter two are more extended (a few arcseconds) and cooler than CH₃CN. Therefore they probe the interface between the extended envelope and the hot core region.
- D/H ratios in the gas phase for methanol (10⁻² ≤ (D/H)_{CH₃OD}^{gas} ≤ 2 × 10⁻³) and water ((D/H)_{HDO}^{gas} ≤ 2.5 ± ^{2.1}_{1.3} × 10⁻³). From the upper limits obtained on the solid observations ((D/H)_{CH₃OD}^{ice} ≤ 3 × 10⁻², (D/H)_{HDO}^{ice} ≤ 6 × 10⁻³), we stress that the CH₃OD/CH₃OH ratio is a good tracer of the enrichment in D of ices when the methanol solid phase abundance can be estimated in the line of sight (which is the case for a few high mass protostars).
- we determine from HCN and HNC data, the existence along the line of sight of two velocity components with different kinetic temperatures. A cool component associated with the main velocity component (< 25K) and a warmer velocity component (> 40K) redshifted from the main cloud.

Acknowledgements. We wish to acknowledge especially R. Neri for many stimulating and fruitful discussions, and a carefull help in the PdBI data reduction.

References

Allamandola L.J., Greenberg J.M., Norman C.A., Hagen W., 1980, IAU Symp. 87, 373
 Bergin E.A., Langer W.D., Goldsmith P.F., 1995, ApJ 441, 222
 Bergin E.A., Neufeld D.A., Melnick G.J., 1998, ApJ 499, 777
 Boogert A.C.A., Ehrenfreund P., Gerakines P.A., et al., 2000, A&A 353, 349
 Boulanger F., Abergel A., Bernard J.-P., et al., 1996, A&A 312, 256

Brown P.D., Millar T.J., 1989, MNRAS 237, 661
 Caselli P., Walmsley C.M., Terzieva R., Herbst E., 1998, ApJ 499, 234
 Charnley S.B., Tielens A.G.G.M., Millar T.J., 1992, ApJ 399L, 71
 Chen N.X., 1990, Phys. Rev. Letters 64, 1193
 Cummins S.E., Thaddeus P., Linke R.A., 1986, ApJS 60, 819
 Dartois E., Demyk K., d'Hendecourt L., Ehrenfreund P., 1999, A&A 351, 1066
 Dartois E., d'Hendecourt L., Boulanger F., et al., 1998, A&A 331, 651
 Gerin M., Wootten H.A., Combes F., et al., 1987, A&A 173, L1
 Guélin M., Langer W.D., Wilson R.W., 1982, A&A 107, 107
 Hagen W., Allamandola L.J., Greenberg J.M., 1980, A&A 86L, 1
 Hasegawa T.I., Herbst E., 1993, MNRAS 263, 589
 Hatchell J., Thompson M.A., Millar T.J., Macdonald G.H., 1998, A&AS 133, 29
 d'Hendecourt L., Jourdain de Muizon M., Dartois E., et al., 1996, A&A 315, L365
 d'Hendecourt L.B., Allamandola L.J., Greenberg J.M., 1985, A&A 152, 130
 d'Hendecourt L.B., 1984, Ph.D. Thesis, University of Leiden
 Herbst E., Leung C.M., 1990, A&A 233, 177
 Hirota T., Yamamoto S., Mikami H., Ohishi M., 1998, ApJ 503, 717
 Jacq T., Walmsley C.M., Henkel C., et al., 1990, A&A 228, 447
 Kessler M.F., Steinz J.A., Anderegg M.E., et al., 1996, A&A 315, L27
 Koike C., Kimura S., Kaito C., et al., 1995, ApJ 446, 902
 Lacy J.H., Baas F., Allamandola L.J., et al., 1984, ApJ 276, 533L
 Langer W.D., Graedel T.E., 1989, ApJS 69, 241
 McCutcheon W.H., Sato T., Dewdney P.E., Purton C.R., 1991, AJ 101, 1435
 McCutcheon W.H., Sato T., Purton C.R., Matthews H.E., Dewdney P.E., 1995, AJ 110, 1762
 Okabe, 1980, Photochemistry of Small Molecules. John Wiley and Sons
 Roueff E., Tiné S., Coudert L.H., Pineau des Forêts G., Falgarone E., Gerin M., 2000, A&A 354, L63
 Schilke P., Walmsley C.M., Pineau Des Forets G., et al., 1992, A&A 256, 595
 Schmitt B., 1993, In: Molecules and grains in space; Proceedings of the AIP Conference, Mont Saint Odile, France 1993, pp. 735-757
 Shah R.Y., Wootten A., 1999, Science with the Atacama Large Millimeter Array (ALMA). Associated Universities, Inc., held October 6-8, 1999 at Carnegie Institution of Washington, E58
 Shalabiea O.M., Caselli P., Herbst E., 1998, ApJ 502, 652
 Shepherd D. S., Churchwell E., 1996, ApJ 457, 267
 Teixeira T.C., Devlin J.P., Buch V., Emerson J.P., 1999, A&A 347, L19
 Tielens A.G.G.M., 1983, A&A 119, 177
 Tielens A.G.G.M., Hagen W., 1982, A&A 114, 245
 Tiné S., Roueff E., Falgarone E., Gerin M. and Pineau des Forêts G., 2000, A&A 356, 1039
 Turner B.E., Terzieva R., Herbst E., 1999, ApJ 518, 699
 Turner B.E., 1990, ApJ 362, L29
 van Dishoeck E.F., Blake G.A., Jansen D.J., Groesbeck T.D., 1995, ApJ 447, 760
 Willacy K., Millar T.J., 1998, MNRAS 298, 562
 Willner S.P., Gillett F.C., Herter T.L., et al., 1982, ApJ 253, 174
 Xie T., Goldsmith P.F., Snell R.L., Zhou W., 1993, ApJ 402, 216